Acta Cryst. (1990). A46, 215-227

Borrmann–Lehmann Interference Patterns in Perfect and in Distorted Crystals

BY A. R. LANG AND G. KOWALSKI*

H. H. Wills Physics Laboratory, University of Bristol, Tyndall Avenue, Bristol BS8 1TL, England

AND A. P. W. MAKEPEACE

Department of Physiology, School of Medicine, University of Bristol, Bristol BS8 1TD, England

(*Received* 20 *February* 1989; *accepted* 10 *October* 1989)

Abstract

The equations of the spherical-wave dynamical diffraction theory for finite polyhedral crystals [Saka, Katagawa & Kato (1972). *Acta Cryst.* A28, 102-113, 113-120] that relate to the Borrmann-Lehmann interference effect have been cast into simple forms in order to display explicitly the leading periodicities and thereby facilitate comparison with experimental observations. The evolution of fringe profiles during passage from the low-absorption case to that of high absorption accompanied by strong anomalous transmission is discussed in detail and illustrated with series of computed profiles. Representative topograph patterns are compared with simulated images and exemplify the poor agreement between observed and calculated fringe spacings previously reported [Lang, Kowalski, Makepeace & Moore (1986). *Acta Cryst.* A42, 501-510]. The effect of lattice distortion in Borrmann-Lehmann interference is investigated by applying the ray-optical diffraction theory for mildly distorted crystals developed by Kato [*J. Phys. Soc. Jpn* (1963), **18**, 1785-1791; (1964), **19**, 67-77, 971-985] with assumption of a constant strain gradient in the specimen. Two factors have been identified that can account for the apparent extreme sensitivity of Borrmann-Lehmann fringe spacings to lattice distortions. One factor arises as a geometrical consequence of the curvature of ray trajectories in the distorted crystals, the other derives from Kato's 'potential' term in the phase integrals of the crystal waves that recombine and interfere. Both factors depend upon the first power of the strain gradient. Under typical experimental conditions, strain gradients sufficiently small as to produce less than 1% contraction in *Pendellösung* fringe spacings can change Borrmann-Lehmann fringe spacings by more than a factor of two.

1. Introduction

Borrmann-Lehmann interference fringes, like the better known *Pendellösung* fringes, are predicted by the dynamical theory of diffraction and may be observed on X-ray topographs of perfect and nearly perfect crystals bounded by appropriately oriented plane facets. In one respect the domain of Borrmann-Lehmann interference phenomena extends beyond that of *Pendellösung* interference because the Borrmann-Lehmann fringe pattern persists with undiminished visibility into the regime of high absorption, when accompanied by anomalous transmission, whereas under these conditions *Pendellösung*-fringe visibility fades away. Early publications of Borrmann-Lehmann fringe patterns exhibited the high-absorption regime, and the observations could be accounted for adequately by a simple dynamical-theoretical treatment involving only the anomalously transmitted waves belonging to branch (1) of the dispersion surface (Borrmann & Lehmann, 1963; Lehmann & Borrmann, 1967). Subsequently it was pointed out by Saka, Katagawa & Kato (1972*a*, *b*) that the 'Laue-Bragg' diffraction geometry under which Borrmann-Lehmann fringes had been generated was just the simplest member of a family of geometries involving Laue-case boundary conditions at the X-ray entrance surface followed by internal reflection at surfaces presenting Bragg-case boundary conditions. All such geometries (in conditions of both high and low absorption) fell within the embrace of these authors' theory of diffraction by finite polyhedral crystals, which was in turn based upon the spherical-wave dynamical theory of X-ray diffraction (Kato, 1961*a*, *b*, 1968).

Observations of Borrmann-Lehmann fringes under conditions of moderately low absorption ($\mu_0 t = 1{\cdot}6$) using polished parallelepiped specimens of diamond and Cu $K\alpha_1$ radiation (recorded a decade ago, Mai & Lang, unpublished) yielded regular fringe patterns of good visibility [a few of which are reproduced in Mai & Zhao (1989)]. In more recent work synchrotron radiation has been employed (Lang, Kowalski, Makepeace & Moore, 1986). In the latter experiments, observations were extended to the case of quite low absorption ($\mu_0 t = 0{\cdot}47$), and patterns were recorded with either σ-mode or π-mode polarizations alone. Use of a single polarization mode facilitated comparison between calculated and observed fringe

* On leave from Institute of Experimental Physics, University of Warsaw, Poland.

0108-7673/90/030215-13$03.00 © 1990 International Union of Crystallography

spacings. Large discrepancies were found (see Table 1 of Lang, Kowalski, Makepeace & Moore, 1986), which were surprising in view of the high perfection of the diamond specimen used as indicated by the regularity of its *Pendellösung* fringe patterns and good agreement between calculated and observed *Pendellösung* period. From such observations arose a major aim of the present work, to investigate factors that may cause spacings of Borrmann-Lehmann fringes to be significantly more sensitive than *Pendellösung* fringe spacings to perturbation by long-range lattice distortions. This subject is introduced after reporting two prior studies. The first concerns computer simulation of topographs of Borrmann-Lehmann fringe patterns. The second deals with changes of the perfect-crystal Borrmann-Lehmann fringe pattern with variation of experimental parameters, and is particularly concerned with the pattern evolution in passing from low-absorption to high-absorption conditions. Changes in the perfect-crystal patterns are illustrated by computed fringe profiles relevant to both previous and likely future experiments with synchrotron radiation.

2. Diffraction geometry

Saka, Katagawa & Kato (1972*a*) provided a classification and terminology applicable within the family of diffraction geometries that includes the configuration leading to Borrmann-Lehmann interference; and additional descriptions, relevant to the present study, appear in Lang *et al.* (1986). In all experiments performed by the latter authors, valuable simplification of the diffraction geometry was gained by using rectangular parallelepiped specimens with symmetrical Laue-case diffraction conditions at the X-ray entrance surface. Figs. 1(*a*) and (*b*) illustrate the two arrangements employed with such specimens when observing Borrmann-Lehmann fringe patterns in the diffracted-beam topograph image. The basic experimental set up was the same as that for taking section topographs with a conventional (Lang, 1957) or synchrotron X-ray source (Lang, 1983). The incident ribbon X-ray beam is limited to a spatial width of about 15 μm by the slit *S* before entering the specimen at the chosen angle. Within the specimen, Bragg diffraction gives rise to crystal waves linked by $\mathbf{k}_g = \mathbf{k}_0 + 2\pi\mathbf{g}$, where $|\mathbf{g}|$ is the reciprocal of the interplanar spacing. To sufficient accuracy for present purposes, the directions of $\mathbf{k}_0$ and $\mathbf{k}_g$ can be taken as those of the incident, $\mathbf{K}_0$, and diffracted, $\mathbf{K}_g$, wave vectors outside the crystal, respectively. To obtain Borrmann-Lehmann interference the parallelepiped specimen is translated with respect to *S* so that the lateral face *FE* cuts into the 'energy-flow triangle' *ORT*. Then Bloch waves excited at *O* can reach the point *W* on the X-ray exit surface *EB* by two paths, either directly along *OW* or by the path *OQ*+*QW* with internal reflection at *Q*. Interference between rays following these two paths generates the Borrmann-Lehmann fringes. To find the distance along *EB* within which rays *OW* and *OQ*+*QW* overlap, the 'image' energy-flow triangle *O'R'T'* is constructed, with *O'R'* parallel to *OR* and *O'T'* parallel

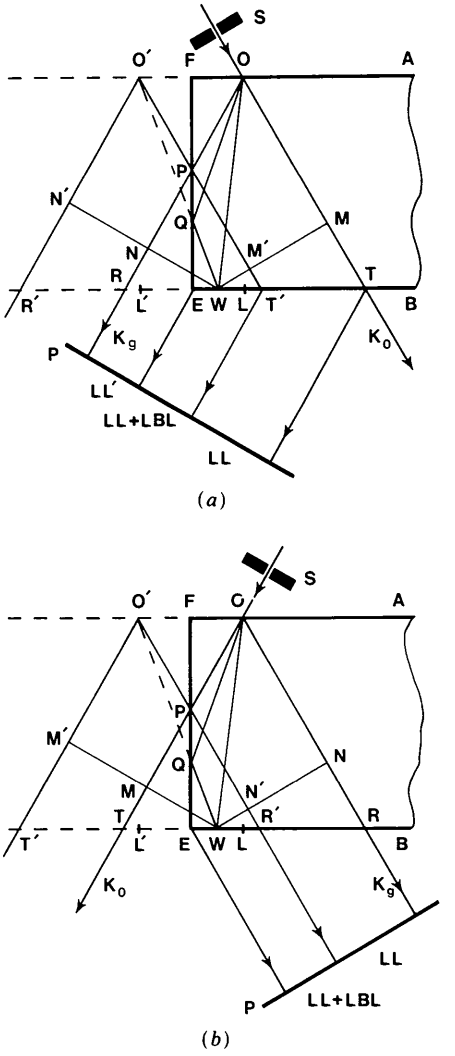

Fig. 1. Plan view on the plane of incidence showing arrangements for recording Borrmann-Lehmann fringes in the diffracted beam ($\mathbf{K}_g$ beam). Specimen crystal parallelepiped shaped with faces *AF*, *FE* and *EB* normal to the plane of incidence. The Bragg planes diffracting are parallel to *FE*. Specimen thickness *FE* = 1 mm. Slit *S* parallel to edges *F* and *E* produces a narrow ribbon X-ray beam impinging at *O*. (X-ray source distance from *S* typically 0·5 m with conventional X-ray tube and 80 m with synchrotron-storage-ring source.) In the triangles *ORT* and *O'R'T'*, *OR* and *O'R'* are parallel to $\mathbf{K}_g$, and *OT* and *OT'* are parallel to $\mathbf{K}_0$. The mid-points of *RT* and *R'T'* are *L* and *L'*, respectively. Distances *FO* = *FO'* = *a*, *EW* = *b*. Perpendicular distances from *W* to *OT* and *OR* are $x_0 = WM$ and $x_g = WN$ respectively, and to *O'T'* and *O'R'* are $x_0' = WM'$ and $x_g' = WN'$ respectively. Borrmann-Lehmann fringes are recorded on photographic plate *P* within the domain *LL*+*LBL*. Experimental settings: (*a*) 'type I', 'negative'; (*b*) 'type II' 'positive'.

to OT. When the Bragg planes and FE are both exactly perpendicular to AF, the apex O' lies on AF prolonged, with $O'F = FO$. The important experimentally variable parameter is the distance $FO = a$. Then with specimen thickness $FE = t$ and Bragg angle θ_B the range of possible Borrmann-Lehmann interference on EB is evidently ET' in Fig. 1(a) and ER' in Fig. 1(b), and is equal to $(t \tan \theta_B - a)$.

In accord with the definitions of Saka *et al.* (1972*a*), rays issuing from the crystal surfaces FE or EB after following a direct path from O are described as undergoing 'Laue-Laue' diffraction, and those after taking the internally reflected path $OQ + QW$ as undergoing 'Laue-Bragg-Laue' diffraction. Thus on plate P Borrmann-Lehmann fringes can be expected in the range designated $LL + LBL$ in Fig. 1, *i.e.* in the range of overlap of Laue-Laue (LL) and Laue-Bragg-Laue (LBL) diffracted rays. Note the difference between the patterns recorded in the arrangement of Figs. 1(a) and (b). In the latter case the image contains only the segment LL due to rays leaving the crystal between R and R' plus the segment $LL + LBL$ due to rays issuing between R' and E. In Fig. 1(a) plate P also receives $\mathbf{K}_g$ waves partially transmitted through the edge FE between P and E. These latter Laue-Laue-case waves produce the image segment distinguished as LL'. The situation in Fig. 1(a), where the lateral face FE cuts the $\mathbf{K}_g$ ray through O, is termed 'type I' Laue-Bragg diffraction by Saka *et al.* (1972*a*) and 'negative case' Laue-Bragg diffraction by Lang *et al.* (1986), with the corresponding terms for the Fig. 1(b) geometry, where FE cuts the $\mathbf{K}_0$ ray through O, termed 'type II' and 'positive case', respectively. Lang *et al.* commend their terminology for a certain mnemonic advantage: in the 'positive case' $\mathbf{g} \cdot \Delta\mathbf{s}$ is positive, where $\Delta\mathbf{s}$ is the change in Poynting vector of the crystal waves on internal reflection at FE.

Fig. 1 shows only the experimental arrangement for recording the $\mathbf{K}_g$-beam image. In fact, with the relatively large Bragg angles usually employed when observing Borrmann-Lehmann patterns, it is possible to obtain complete spatial separation of the full widths of diffracted and transmitted beams without requiring specimen-to-plate distances of more than a few centimetres. Thus the $\mathbf{K}_0$-beam and $\mathbf{K}_g$-beam images can be recorded simultaneously. The experimental arrangements for so doing are explained in Fig. 1 of Lang *et al.* (1986), and both $\mathbf{K}_0$-beam and $\mathbf{K}_g$-beam Borrmann-Lehmann fringe patterns are exhibited in that paper.

3. Theory for perfect crystals

All needed expressions for wave amplitudes on the X-ray exit surfaces of the specimen have been derived by Kato and co-workers through development of the spherical-wave dynamical diffraction theory for perfect crystals. The following treatment proceeds from their equations. Attention will be restricted to the diffracted wave (G wave), and diffraction in a single polarization mode will be implicit in most discussion of fringe visibility *etc.* To introduce the notation, consider first the amplitude of the G wave, $d_g(\mathbf{r})$, at points within the energy-flow triangle ORT in the absence of reflections from lateral surfaces. Spherical-wave theory gives $d_g(\mathbf{r})$ as

$$d_g(\mathbf{r}) = \beta J_0(\rho), \tag{1}$$

after eliminating some constant phase and amplitude factors from the expressions of Kato [1968, equation (34); 1974, equation (4-205b)]. Here β is proportional to the strength of the reflection [Saka *et al.*, 1972*a*, equation (9); Kato, 1974, equation (4-55c)] and $\rho = \beta (x_0 x_g)^{1/2}$. The coordinates x_0 and x_g are the perpendicular distances of the point $\mathbf{r}$ from the $\mathbf{K}_0$ and $\mathbf{K}_g$ edges of the energy-flow triangle ORT, respectively (see Fig. 1). With symmetrical-Laue-case conditions at the X-ray entrance surface, equivalent expressions for β are

$$\beta = KC(\chi_g \chi_{-g})^{1/2} / \sin 2\theta_B \tag{2a}$$

and

$$\beta = \pi / \xi_g \sin \theta_B. \tag{2b}$$

In equation (2a), $K = 2\pi/\lambda$, C is the polarization factor and χ_g is the gth Fourier coefficient of the polarizability of the crystal for X-rays. In (2b), ξ_g is the extinction distance, *i.e. Pendellösung* period parallel to the Bragg planes. If the crystal is absorbing, β and ξ_g^{-1} are complex. The relation between the real part of ξ_g^{-1} and the real part of the structure factor F_g is $\xi_g^{-1} = (e^2/mc^2)|F_g|C\lambda/\pi V \cos\theta_B$, V being the volume of the unit cell.

When the triangle ORT is cut by the lateral surface FE, imposition of the surface boundary conditions on the Poynting vector of the crystal waves requires that either the G wave or the 0 wave be totally reflected at the surface. In Fig. 1(a) the 0 wave is totally reflected, and in Fig. 1(b) the G wave. In their spherical-wave analysis, Saka *et al.* show that the crystal wave field resulting from such reflection is identical to that obtained with addition of a second energy-flow triangle, subtended from a virtual entry point O'. The simple construction locating O' in Fig. 1 follows from the particularly simple diffraction geometry under present consideration. The image received on the plate P is the projection along $\mathbf{K}_g$ of the intensity distribution over the exit surface that is the resultant of G waves belonging to the two triangles ORT and $O'R'T'$. From the expressions for G-wave amplitudes over ET in the positive case, type II, and over PE and ET in the negative case, type I, the component amplitudes, D_g, in the several image domains identified on P in Fig. 1 can be expressed in the following simplified forms, after eliminating

the multiplying factor β common to all. For the positive case, type II, the amplitudes are

$$D_g^{LL} = J_0(\rho) = J_0[\beta(x_0 x_g)^{1/2}], \qquad (3a)$$

and

$$D_g^{LBL} = -J_0(\rho') = -J_0[\beta(x_0' x_g')^{1/2}], \qquad (3b)$$

giving in the domain of the Borrmann-Lehmann interference pattern simply

$$D_g^{LL+LBL} = J_0(\rho) - J_0(\rho'). \qquad (3c)$$

In the negative case, type I, the same expression for D_g^{LL} applies, but

$$D_g^{LBL} = (x_0'/x_g')J_2(\rho'), \qquad (4a)$$

so that

$$D_g^{LL+LBL} = J_0(\rho) + (x_0'/x_g')J_2(\rho'). \qquad (4b)$$

The amplitude in the domain LL' is

$$D_g^{LL'} = J_0(\bar{\rho}) + (\bar{x}_g/\bar{x}_0)J_2(\bar{o}). \qquad (4c)$$

In the above, coordinates and parameters relating to the triangle $O'R'T'$ are primed, and x_0, x_g, x_0' and x_g' are the coordinates of points on the surface EB. In the expression for $D_g^{LL'}$, an overbar distinguishes values on PE. Sources of these equations are: (3b) from Saka *et al.* (1972a), equation (52b); Kato (1974), equation (4-244b); (4a) from Saka *et al.* 1972a), equation (50b); Kato (1974), equation (241b); and (4c) from Kato (1974), equation (4-242a).

Under all experimental conditions employed to date, the arguments ρ, ρ' and $\bar{\rho}$ are large. Hence asymptotic forms of the Bessel functions may be used. In the non-absorbing limit the equations above further simplify, and after elimination of common factors become, for the positive case, type II,

$$D_g^{LL} = (x_0 x_g)^{-1/4} \cos(\rho - \pi/4), \qquad (5a)$$

and

$$D_g^{LBL} = -(x_0' x_g')^{-1/4} \cos(\rho' - \pi/4), \qquad (5b)$$

giving

$$D_g^{LL+LBL} = (x_0 x_g)^{-1/4} \cos(\rho - \pi/4) - (x_0' x_g')^{-1/4} \cos(\rho' - \pi/4). \qquad (5c)$$

In the negative case, type I, equations (4a) and (4c) reduce to

$$D_g^{LBL} = -(x_0'/x_g')(x_0' x_g')^{-1/4} \cos(\rho' - \pi/4) \qquad (6a)$$

and

$$D_g^{LL'} = (\bar{x}_0 \bar{x}_g)^{-1/4}(1 - \bar{x}_g/\bar{x}_0) \cos(\bar{\rho} - \pi/4), \qquad (6b)$$

producing, in the Borrmann-Lehmann interference domain,

$$D_g^{LL+LBL} = (x_0 x_g)^{-1/4} \cos(\rho - \pi/4) - (x_0'/x_g')(x_0' x_g')^{-1/4} \cos(\rho' - \pi/4). \qquad (6c)$$

Equations (5c) and (6c) make it obvious that for each polarization mode four-wave interference occurs in the $LL+LBL$ domain, the resultant of coherent superposition of the two-wave *Pendellösung* interference systems proper to both ORT and $O'R'T'$. Comparison of the expressions for D_g^{LL+LBL} in (5c) and (6c) shows why it is preferred experimentally to record Borrmann-Lehmann fringes in the positive case, type II setting, since in (5c) the terms in ρ and ρ' have more equal weighting. At E, $x_0 x_g = x_0' x_g'$; also, $(x_0 x_g)^{-1/4}$ and $(x_0' x_g')^{-1/4}$ are slowly varying over ER' except near R' where $(x_0' x_g')^{-1/4}$ rises sharply. Hence there will be little error over most of ER' in approximating (5c) by

$$D_g^{LL+LBL} \simeq \cos(\rho - \pi/4) - \cos(\rho' - \pi/4), \qquad (7)$$

yielding the intensity distribution (for each polarization mode)

$$|D_g^{LL+LBL}|^2 \simeq 4 \sin^2 \tfrac{1}{2}(\rho + \rho' - \pi/2) \sin^2 \tfrac{1}{2}(\rho - \rho'). \qquad (8)$$

For comparison with this zero-absorption expression, consider the case of very high absorption with strong anomalous transmission. In the expansion

$$J_0(\rho) \propto (x_0 x_g)^{-1/4}[\exp i(\rho - \pi/4) + \exp -i(\rho - \pi/4)]$$

the positive and negative exponents represent respectively the branch (1) and branch (2) waves, here adopting the exponent sign convention $\exp i[\mathbf{k}.\mathbf{r} - \omega t)$ for a progressive wave, as done by Kato. Only the branch (1) wave need now be considered, so that (7) transforms to

$$D_g^{LL+LBL} \simeq \exp(-i\pi/4)[\exp(i\rho) - \exp(i\rho')] \qquad (9)$$

which yields the intensity distribution

$$|D_g^{LL+LBL}|^2 \simeq 4 \sin^2 \tfrac{1}{2}(\rho - \rho'). \qquad (10)$$

Equation (10) is just the expression for Borrmann-Lehmann fringes that comes out of simple wave-vector-difference calculations from dispersion-surface geometry in the high-absorption case (Borrmann & Lehmann, 1963; Lehmann & Borrmann, 1967; Lang *et al.*, 1986). Analysis of situations intermediate between the extremes of (8) and (10) is pursued later, in § 5.

For comparing observations with theory it is convenient to replace the coordinates x_0 *etc.* of the point W distant b from E by the parameters σ and σ' (Kato, 1968) defined by $\sigma = \mathbf{LW}/\mathbf{LR}$ and $\sigma' = \mathbf{L'W'}/\mathbf{L'R'}$. When symmetrical Laue conditions apply at entrance and exit surfaces, $x_0 = t(1+\sigma)\sin\theta_B$ and $x_g = t(1-\sigma)\sin\theta_B$, giving

$$(x_0 x_g)^{1/2} = t(1-\sigma^2)^{1/2} \sin\theta_B,$$

with corresponding relations between x_0', x_g' and σ'. Also resulting from the simple geometry assumed is the identity of σ with the important energy-flow

parameter $p = \tan\Theta/\tan\theta_B$, in which Θ is the angle between Poynting vector and Bragg plane. Consider first the predictions of fringe position in the high-absorption case (10), when various levels of approximation are allowed in expanding $(\rho - \rho')$. Substitution of $p = \sigma$, $p' = \sigma'$ and use of (2*b*) gives

$$\rho - \rho' = \pi t \xi_g^{-1}[(1-p^2)^{1/2} - (1-p'^2)^{1/2}], \quad (11a)$$

which becomes

$$\rho - \rho' = \pi t \xi_g^{-1}\{[1-(p_E - B)^2]^{1/2} - [1-(p_E + B)^2]^{1/2}\} \quad (11b)$$

upon introducing $p_E = a/t \tan\theta_B$ and $B = b/t \tan\theta_B$. Substitution of the abbreviations

$$R = [1-(p_E - B)^2]^{1/2}$$

and $R' = [1-(p_E + B)^2]^{1/2}$, and differentiation of their difference with respect to B gives

$$\mathrm{d}(R - R')/\mathrm{d}B = 2p_E \quad (12a)$$

under the approximation that $(p_E \pm B)^2$ can be neglected relative to unity. With retention of p_E^2 and B^2, (12*a*) becomes

$$\mathrm{d}(R - R')/\mathrm{d}B = 2p_E(1-p_E^2)^{-1/2}[1 + \tfrac{1}{2}B^2(1-p_E^2)^{-1}]. \quad (12b)$$

Let Δ_a denote the Borrmann-Lehmann fringe spacing at W. Then the increment $\Delta B = \Delta_a/t \tan\theta_B$ corresponds to the increment $\Delta(\rho - \rho') = 2\pi$ in (10). Combination of (11*b*) and (12*a*) thus gives

$$\Delta_a = \xi_g (t/a) \tan^2\theta_B, \quad (13)$$

recognizable as the simple formula for fringe spacing in the high-absorption case when both a and b are small compared with $t \tan\theta_B$ [Borrmann & Lehmann, 1963; Lang *et al.*, 1986, equation (5*a*)]. Corrections that can be applied to (13) when a and/or b are not small compared with $t \tan\theta_B$ follow from (12*b*).

4. Experiment and simulation

Computations of fringe profiles needed for simulations were made without approximations in (3) and (4) other than replacement of Bessel functions by their asymptotic expansions and the usual assumption that the ratio of imaginary to real part of the polarizability is very small. Anomalous absorption is handled conventionally, as follows. The effective absorption factor for a ray reaching EB from O along direction p is

$$\exp\{(-\mu_0 t \sec\theta_B)[1 \pm C \exp(-M)\varepsilon(1-p^2)^{1/2}]\},$$

in which μ_0 is the normal linear absorption coefficient, $\exp(-2M)$ is the Debye-Waller factor for intensities, and ε is the ratio χ_g''/χ_0'', *i.e.* the ratio of the imaginary parts of the polarizability for orders g and 0. The positive and negative signs apply to branch (2) and branch (1) waves respectively. The factor $\exp(-\mu_0 t \sec\theta_B)$ uniformly attenuates all rays, and can be eliminated. Hence in the formal replacement of ρ by $\rho_r - i\rho_i$ to take account of absorption, only the anomalous component need be included in ρ_i. This is conveniently done by introducing the imaginary part of the extinction distance, which is given by $(2\pi/\xi_g^i) = C \exp(-M)\varepsilon\mu_0 t \sec\theta_B$. Retaining ξ_g to denote the real part of the extinction distance, the real and imaginary parts of ρ are thus

$$\rho_r = \pi t(1-p^2)^{1/2}/\xi_g \quad (14a)$$

and

$$\rho_i = \pi t(1-p^2)^{1/2}/\xi_g^i \quad (14b)$$

with corresponding relations involving ρ_r', ρ_i' and p'. To illustrate application of (14*a*) and (14*b*), consider (5*a*), which for complex ρ becomes

$$D_g^{LL} = (1-p^2)^{-1/4}[\cos(\rho_r - \pi/4)\cosh\rho_i + i\sin(\rho_r - \pi/4)\sinh\rho_i], \quad (15)$$

and yields the intensity distribution

$$|D_g^{LL}|^2 = (1-p^2)^{-1/2}\{\cos^2[\pi t(1-p^2)^{1/2}/\xi_g - \pi/4] + \sinh^2[\pi t(1-p^2)^{1/2}/\xi_g^i]\}. \quad (16)$$

Equation (16) recognizably gives the intensity profile across a section topograph of an absorbing perfect crystal in the symmetrical Laue case (omitting constant factors), expressed as a function of p. Intensity profiles of Borrmann-Lehmann fringe patterns with any magnitude of anomalous absorption are derived straightforwardly. For example, in the type II (positive) setting, (5*c*) gives for $|D_g^{LL+LBL}|^2 = I_{BL}$ the equivalent expressions

$$I_{BL} = |D_g^{LL}|^2 + |D_g^{LBL}|^2 + 2\,\mathrm{Re}[(D_g^{LL})(D_g^{LBL})^*] \quad (17a)$$

or

$$I_{BL} = [\mathrm{Re}(D_g^{LL} + D_g^{LBL})]^2 + [\mathrm{Im}(D_g^{LL} + D_g^{LBL})]^2. \quad (17b)$$

Using the link $p' = p \pm 2p_E$, plots of I_{BL} *vs* p (or B) have been computed, inserting appropriate values of ξ_g and ξ_g^i and of other parameters such as a that have been deliberately experimentally varied (Kowalski & Lang, 1987).

Representative comparisons between experiment and simulation are shown in Figs. 2 and 3. The topographs illustrate differences between the type I (negative-setting) pattern, Fig. 2, and the type II (positive-setting) pattern, Fig. 3. Furthermore, the topograph in Fig. 2 was taken with Cu $K\alpha_1$ radiation whereas that in Fig. 3 was obtained using synchrotron radiation, the Bragg angle being set so that radiation of wavelength 0·15 nm underwent the 220 reflection. Fig. 2(*a*) shows a 0·45 mm high segment of the image of a parallelepiped crystal whose edge E stood 5 mm

high normal to the plane of incidence. It reproduces part of Fig. 2 of Lang *et al.* (1986), wherein leading features of the pattern were described, including evidence of perturbations by lattice imperfections. Other points to note, relevant to the comparison with simulation, are as follows. Fig. 1(*a*) explains the geometry of Fig. 2(*a*); and the position of the image of *E*, coinciding with the left-hand limit of the Borrmann–Lehmann fringe domain, is immediately recognizable. Reference to Fig. 1(*a*) shows that the widths of the Borrmann–Lehmann fringe domain to the right of *E* and of the *LL'* domain to the left of *E* are identical. From (4*a*), (4*b*), (6*a*) and (6*b*), it is seen that the amplitude of D_g^{LBL} decreases monotonically from *E* to *T'*, the factor $x_0'/x_g' = (1+p')/(1-p')$ falling to zero at *T'* where $p' = -1$. Consequently, the (*LL*+*LBL*) pattern merges smoothly with the normal *Pendellösung* (*LL*) pattern at the position on *P* corresponding to the image of *T'*. On the simulation this merging can be traced, but on the topograph the Borrmann–Lehmann fringe visibility vanishes closer to *E*. The maximum *Pendellösung* fringe spacing on *P* just to the left of the image of *E*, in the *LL'* domain, is 11·5 μm, and is less than the incident-beam width of about 15 μm, which is determined principally by the opening of *S*. Consequently, individual *Pendellösung* fringes in *LL'* are not resolved; but there can be recognized a periodic variation in the photographically recorded intensity resulting from the superimposition of the *Pendellösung* fringe patterns produced by the σ- and π-polarization modes (Hart & Lang, 1965; Hattori, Kuriyama & Kato, 1965).

The systems employed for computer simulation of the images, and for photography of the simulations, were essentially those previously developed for simulating section topograph patterns of crystals containing stacking faults (Kowalski & Lang, 1986). The pixel sizes corresponded to a width of 1·25 μm on the plate *P* in Fig. 2(*b*), and less in the case of Fig. 3(*b*), and so were well below the minimum fringe spacing likely to be resolved experimentally. When dealing with unpolarized radiation, the σ and π patterns were calculated separately, and added together in appropriate ratio in the display to be photographed, thus correctly simulating the diffraction conditions, and producing the periodic fading of *Pendellösung* fringe visibility seen in Fig. 2(*b*). Adopting the structure-factor value $F_{220} = 15{\cdot}39$ from Dawson (1967), the spacing on *P* of the leading Borrmann–Lehmann fringes, calculated for the high-absorption limit *via* (12*b*), and setting $|p| = p_E$, is 44·5 μm for the dominant σ-polarization mode. In the topograph segment shown, the average fringe spacing of the few fringes clearly observed is roughly 30% smaller. Elsewhere along the same crystal edge the spacing falls to less than half the calculated value,

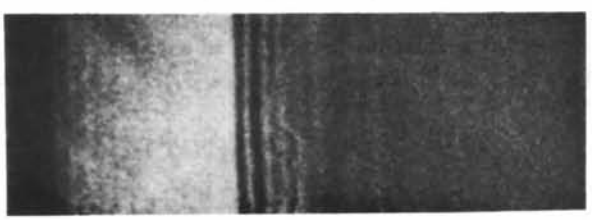

(*a*)

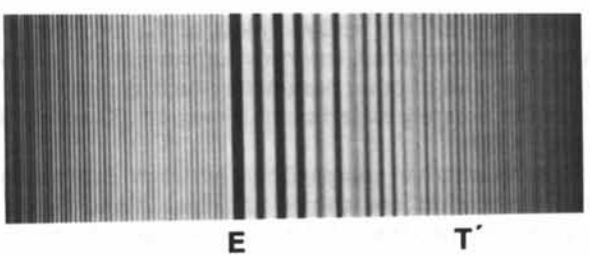

(*b*)

Fig. 2. Observed and simulated $\mathbf{K}_g$-beam section topographs showing Borrmann–Lehmann fringes in the type I (negative) setting (*cf.* Fig. 1*a*). Radiation Cu $K\alpha_1$, 220-type reflection, $2\theta_B = 75°$, crystal thickness $t = 1$ mm, $\mu_0 t = 1{\cdot}6$, $a = 0{\cdot}18$ mm, $p_E = 0{\cdot}23$. Full width of section image is shown (1·25 mm on *P*). (*a*) Segment 0·45 mm high of topograph image. (*b*) Simulation of (*a*).

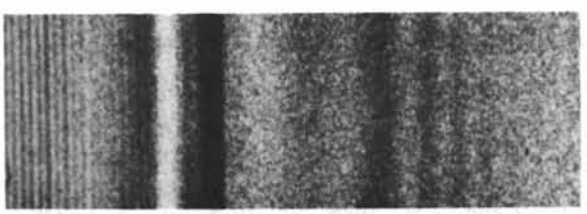

(*a*)

(*b*)

Fig. 3. (*a*) Observed and (*b*) simulated $\mathbf{K}_g$-beam section topographs showing Borrmann–Lehmann fringes in the type II (positive) setting (*cf.* Fig. 1*b*). Synchrotron radiation, σ-polarization mode, $\lambda = 0{\cdot}15$ nm, 220-type reflection, $2\theta_B = 73°$, $t = 1$ mm, $\mu_0 t = 1{\cdot}6$, $a = 0{\cdot}44$ mm, $p_E = 0{\cdot}56$. Height of image = 0·23 mm. The width of image reproduced is centred on $p = 0$, and spans the range $-0{\cdot}56 \le p \le 0{\cdot}56$. Thus the left-hand limit is the image of edge *E*, and on the right the *LL* domain between $p = 0{\cdot}56$ and $p = 1$ is excluded. Fringe spacings on *P* near image of edge *E*: (*a*) 9·4 μm, (*b*) 14·7 μm.

despite constancy of a and t. Regarding absorption, $\exp(-M)$ does not significantly differ from unity at room temperature in the case of diamond. The simulations Figs. 2(b) and 3(b) were computed assuming an ideally perfect diamond, free from static lattice disorder, and the value $\varepsilon = 0{\cdot}96$ was adopted for the 220 reflection in this case. Under such conditions only minor perturbations of fringe positions and intensities from those produced in the high-absorption limit appear.

A characteristic feature of type II (positive-setting) patterns, when absorption is low or moderate, is the pile up of intensity on approaching the ray $O'R'$ from within the triangle $T'O'R'$. In the pattern reproduced in Fig. 3(a) [also shown, and used for structure-factor measurement, in Lang *et al.* (1986)], this intensity peak corresponding to the image of R' stands out very strongly. Its contrast appears all the greater by virtue of proximity to a pronounced intensity minimum lying about 50 μm on its left. This minimum, and oscillations of mean intensity flanking it, are attributable to bending of ray trajectories caused by strain gradients in the specimen. Unfortunately, the distribution and magnitude of these gradients cannot be inferred directly from the intensity distribution on the image. In the synchrotron-radiation topograph the contrast of *Pendellösung* fringes in the LL domain vanishes near the right-hand edge of the pattern. Consequently, that uninteresting strip of image has been excluded from reproduction so as to allow greater enlargement of the Borrmann–Lehmann fringe pattern close to the left-hand edge. The part of the image included in Figs. 3(a) and (b) is symmetrical about $p = 0$ and covers the range $-p_E \le p \le p_E$, with $p_E = 0{\cdot}56$ in this experiment. The fringe pattern exemplifies those obtained with a relatively high value of p_E. Patterns can be classified according to whether or not a is greater than ET' in Fig. 1(a) [or ER' in Fig. 1(b)], *i.e.* whether or not p_E is greater than 0·5. In Fig. 3(a), where a is greater, the central fringe of the normal *Pendellösung* pattern is included in the LL domain. Parameters used in the simulation have been adjusted to produce a fair match with the *Pendellösung* phase at $p = 0$ in the topograph. Such adjustment is permissible since with high-order *Pendellösung* interference ($t/\xi_g \simeq 60$ for $\lambda = 0{\cdot}15$ nm), uncertainties of less than 1% in θ_B, t or ξ_g correspond to fringe shifts of a substantial fraction of an order. In the $LL + LBL$ domain the large-scale intensity oscillations referred to above warn that the crystal is not as free from strain gradients as the good visibility and regularity of the Borrmann–Lehmann fringe pattern might lead the observer to believe. Departure from ideal behaviour is revealed strikingly by the large difference between Borrmann–Lehmann fringe spacings seen in topograph and simulation, the ratio of calculated to observed spacings being as high as 1·6 in this example.

5. Pattern evolution with changes of wavelength and absorption

Plots of diffracted intensity *vs* the parameter p are informative for demonstrating variations of positions and intensity of individual fringes that occur under low absorption conditions, and for tracing the evolution of the fringe pattern towards the high-absorption limit. Since the majority of experiments were performed in the type II (positive) setting, and in all synchrotron-radiation experiments only the $\mathbf{K}_g$ beam was recorded, these conditions have been assumed in the plots shown here. The synchrotron-radiation experiments on diamond with $\lambda = 0{\cdot}1$ nm exemplify low-absorption conditions. Complete section topograph intensity profiles computed from (16) and (17) are shown in Fig. 4. The choice $p_E = 0{\cdot}3$ represents typical experimental conditions. As already pointed out, small changes of a, t or θ_B (and hence of λ and ξ_g) will substantially change the *Pendellösung* phase at $p = p_E$. Figs. 4(a)–(d) illustrate four epochs within

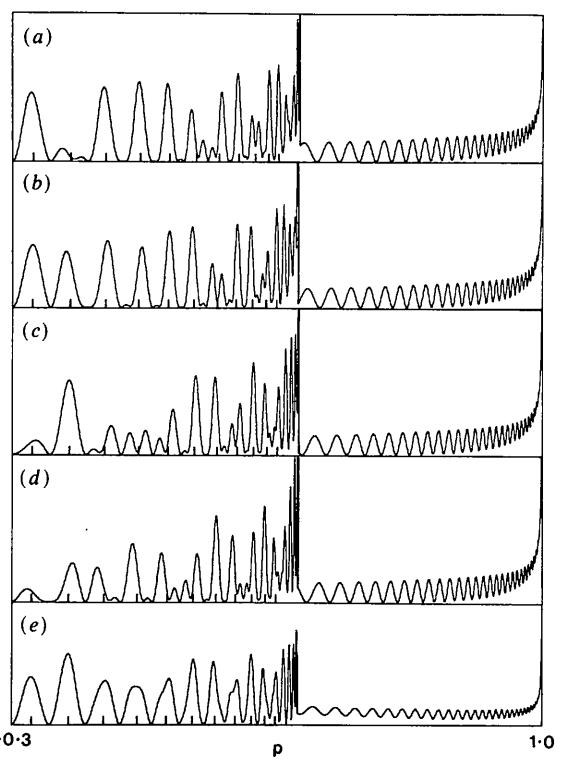

Fig. 4. Computed complete section topograph intensity profiles containing Borrmann–Lehmann fringes, left, and normal *Pendellösung* fringes, right. Type II (positive) setting, *cf.* Fig. 1(b). Abscissa range $-0{\cdot}3 \le p \le 1{\cdot}0$, $p_E = 0{\cdot}3$. (Corresponding actual section image width on plate P when $\lambda = 0{\cdot}1$ nm and $t = 1$ mm is 0·52 mm.) Polarization σ mode in all plots. Ordinates: relative intensity on linear scale. Abscissa ticks indicate positions of first 11 Borrmann–Lehmann fringe maxima in high-absorption limit. (a)–(d) Absorption as in diamond, $\xi_g^i = 18{\cdot}3$ mm; *Pendellösung* phase $t/\xi_g = 34{\cdot}0$, 34·25, 34·5 and 34·75, respectively. (e) Diamond absorption ×6, $\xi_g^i = 3{\cdot}0$ mm; $t/\xi_g = 34{\cdot}5$.

a cycle of unit increment in t/ξ_g. The ticks along the abscissa axes show where Borrmann-Lehmann fringe maxima would appear in the high-absorption limit for the respective values of t/ξ_g. Fig. 4(*e*) represents a hypothetical specimen possessing six times the absorption of diamond. [The term 'absorption' in the present context means the product $C\varepsilon \exp(-M)\mu_0 t_0 \sec\theta_B$.] Observe that whereas absorption reduces the visibility of the normal *Pendellösung* fringe pattern in the *LL* domain, the visibility of the Borrmann-Lehmann fringes remains unimpaired in most of their domain. The specimen used was known to contain imperfections in the form of point defects and submicroscopic platelets on {100}, and evidence from double-crystal difractometric measurement of the angular width of the 220 reflection (publication in preparation) indicated the value $\varepsilon = 0{\cdot}7$, which was that adopted in the computations.

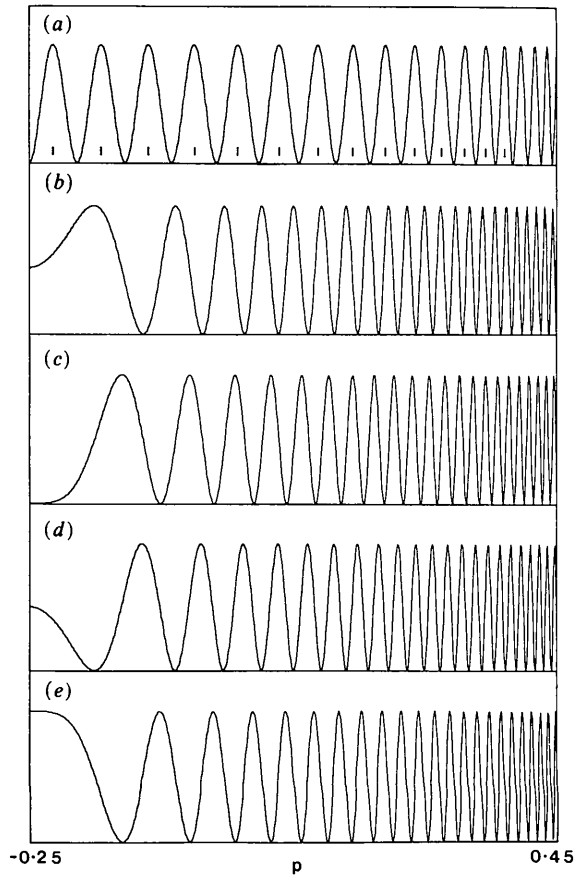

Fig. 5. The 'sum' and 'difference' intensity functions whose product forms the zero-absorption Borrmann-Lehmann fringe pattern in the type II (positive) setting, under the approximation $(1-p^2)=(1-p'^2)=1$. In all plots $p_E = 0{\cdot}25$, and the abscissa range is $-0{\cdot}25 \le p \le 0{\cdot}45$. (*a*), I^-, $t/\xi_g = 60$. Ticks show positions of Borrmann-Lehmann fringe maxima in the high-absorption limit. (*b*)-(*e*) I^+, with values of ρ_r and ρ'_r at E being respectively $57{\cdot}75\pi$, $58{\cdot}0\pi$, $58{\cdot}25\pi$ and $58{\cdot}5\pi$ (corresponding to $t/\xi_g \simeq 60$ at $p = 0$).

Borrmann-Lehmann fringe patterns produced with the longer wavelength, 0·15 nm, and consequent increase of t/ξ_g to about 60 with the 1 mm thick specimen, will now be considered, first examining how the pattern variability that occurs under low-absorption conditions is generated [already shown in Figs. 4(*a*)-(*d*)]. For this purpose it is helpful to refer to the plots in Fig. 5 of the basic 'sum' and 'difference' functions whose product forms the fringe pattern in the low-absorption case, (8), when the slowly varying amplitude factors $(1-p^2)^{-1/4}$ and $(1-p'^2)^{-1/4}$ are both approximated by unity. In Fig. 5 the difference function I^- is $\sin^2\frac{1}{2}(\rho_r - \rho'_r)$, the sum function I^+ is simplified to $\sin^2\frac{1}{2}(\rho_r + \rho'_r)$, $p_E = 0{\cdot}25$ and the plots are truncated on the right-hand side at $p = 0{\cdot}45$ (*i.e.* $p' = 0{\cdot}95$) to exclude rapid oscillations unlikely to be resolved experimentally. The function I^- (Fig. 5*a*), which represents the high-absorption Borrmann-Lehmann fringe pattern, is always anchored to the edge E ($p = -0{\cdot}25$) with a minimum at that point. The four sum functions in Figs. 5(*b*)-(*e*) represent values of $\frac{1}{2}(\rho_r + \rho'_r)$ at E increasing in steps of $\pi/4$. Figs. 6-9 show the full calculations of Borrmann-

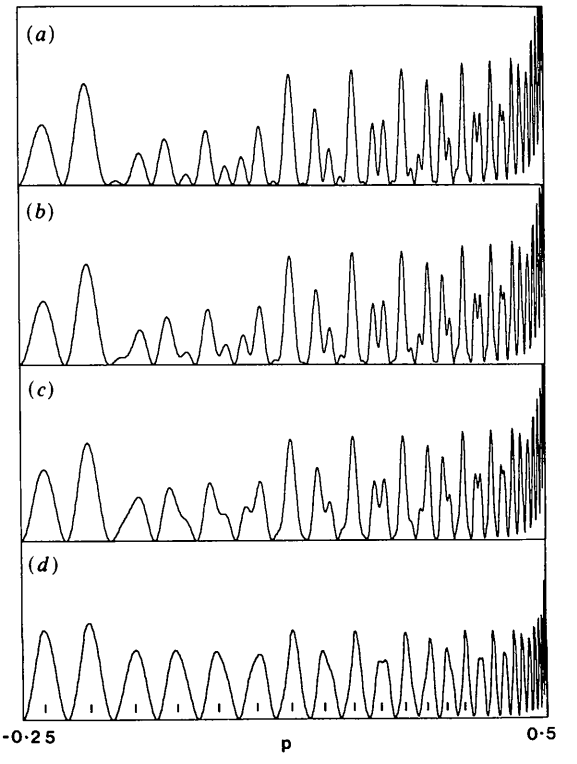

Fig. 6. Variation of Borrmann-Lehmann fringe patterns with increasing absorption. Type II (positive) setting, $t/\xi_g \simeq 60$, $p_E = 0{\cdot}25$, abscissa range $-0{\cdot}25 \le p \le 0{\cdot}5$, corresponding to range from E to R' on exit surface. Case when ρ_r and $\rho'_r = 57{\cdot}75\pi$ at E, *cf.* Fig. 5(*b*). (*a*)-(*d*) $t/\xi'_g = 0$, 0·104, 0·208 and 0·417, respectively. (*c*) corresponds to diamond with $\lambda = 0{\cdot}15$ nm, $t = 1$ mm, σ polarization and $\varepsilon = 0{\cdot}7$. In (*d*), ticks show positions of first 14 fringe maxima in high-absorption limit.

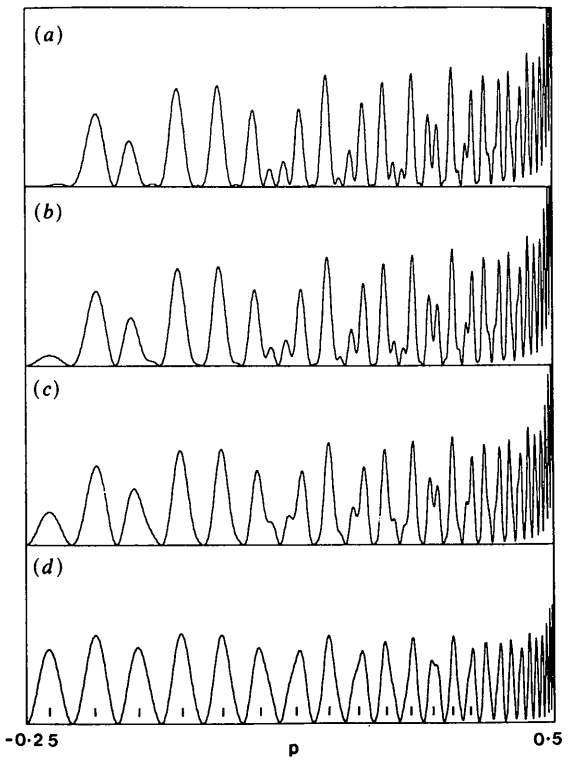

Fig. 7. (*a*)-(*d*) As Fig. 6, but with ρ_r and $\rho'_r = 58{\cdot}0\pi$ at *E*. Compare with Fig. 5(*c*).

Lehmann fringe patterns for $\lambda = 0{\cdot}15$ nm, $p_E = 0{\cdot}25$, with t/ξ_g values corresponding to the four phases of I^+ at *E* in Figs. 5(*b*)-(*e*), and with ξ_g^i spanning the range from zero to high absorption. All the Borrmann-Lehmann fringe domain is included ($-0{\cdot}25 \leq p \leq 0{\cdot}5$), but not the normal *Pendellösung* domain at higher *p*, *i.e.* $0{\cdot}5 \leq p \leq 1$. In each of Figs. 6-9 the plots (*a*) to (*d*) are for $\xi_g^i = \infty$, 9·6, 4·8 and 2·4 mm, respectively. The value $\xi_g^i = 4{\cdot}8$ mm applies to diamond at $\lambda = 0{\cdot}15$ nm with $\varepsilon = 0{\cdot}7$. The abscissa ticks show positions of the first fourteen fringe maxima in the high-absorption limit for each value of the parameter t/ξ_g assumed. To understand the fringe profiles produced at the lower absorptions, refer to the corresponding product of I^+ and I^- in Fig. 5. Thus, for example, Fig. 6(*a*) is seen as the product of the curves of Fig. 5(*a*) and Fig. 5(*b*), disregarding a very small fractional difference in t/ξ_g between Figs. 5(*a*) and 6(*a*) and the omission of the amplitude factors $(1-p^2)^{-1/4}$ and $(1-p'^2)^{-1/4}$ in Fig. 5.

The transformation of the profile I_{BL} by absorption is clearly exposed if in addition to approximating $(1-p^2)^{-1/4}$ and $(1-p'^2)^{-1/4}$ by unity a further approximation is made by assuming that the equality of ρ_i and ρ'_i existing at *E* also extends throughout the Borrmann-Lehmann fringe region of interest. Then, introducing $\bar{\rho}_i = \frac{1}{2}(\rho_i + \rho'_i)$ and dividing by

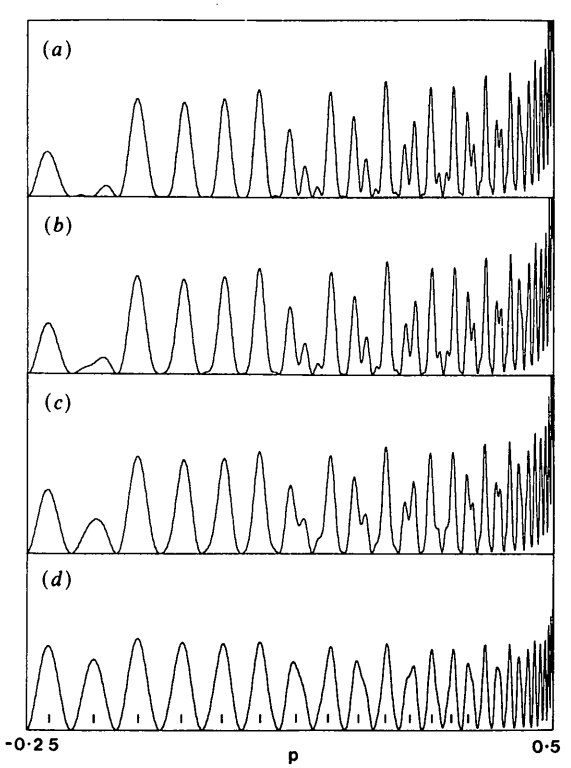

Fig. 8. (*a*)-(*d*) As Fig. 6, but with ρ_r and $\rho'_r = 58{\cdot}25\pi$ at *E*. Compare with Fig. 5(*d*).

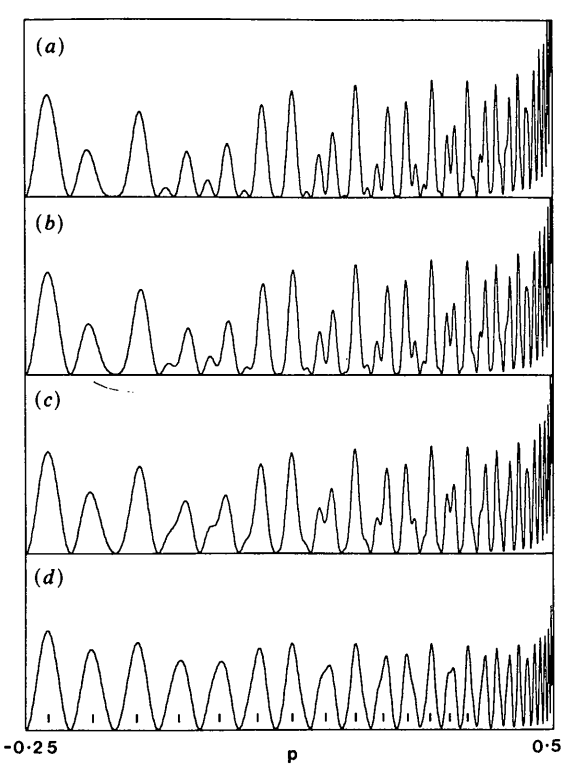

Fig. 9. (*a*)-(*d*) As Fig. 6, but with ρ_r and $\rho'_r = 58{\cdot}5\pi$ at *E*. Compare with Fig. 5(*e*).

$\cosh \bar{\rho}_i$, (15) becomes

$$D_g^{LL} \simeq \cos(\rho_r - \pi/4) + i \tanh \bar{\rho}_i \sin(\rho_r - \pi/4), \tag{18}$$

with a correspondingly simplified expression for D_g^{LBL}. Inserting these expressions in (17*b*) gives

$$I_{BL} = [\cos(\rho_r - \pi/4) - \cos(\rho_r' - \pi/4)]^2 + \tanh^2 \bar{\rho}_i [\sin(\rho_r - \pi/4) - \sin(\rho_r' - \pi/4)]^2$$

which transforms to

$$I_{BL} = 4 \sin^2 \tfrac{1}{2}(\rho_r - \rho_r')[\sin^2 \tfrac{1}{2}(\rho_r + \rho_r' - \pi/2) \times (1 - \tanh^2 \bar{\rho}_i) + \tanh^2 \bar{\rho}_i]. \tag{19}$$

Equation (19) shows that under the approximations adopted the fringe profile for any value of absorption is an appropriately weighted mean of the zero-absorption profile (8) and the high-absorption profile (10).

6. Strained crystals

This final section addresses the question why large discrepancies between calculated and observed Borrmann-Lehmann fringe spacings may be observed in nearly perfect crystals whose *Pendellösung* patterns give no indication of significant perturbation by strain gradients. It seeks to identify factors peculiar to the diffraction geometry of Borrmann-Lehmann interference that confer great sensitivity to lattice distortion. Dynamical X-ray diffraction theories developed for strained crystals can be differentiated into those attacking from a wave-optical or from a ray-optical viewpoint. In the former category are the theories of Takagi (1962, 1969) and Taupin (1964), and in the latter those of Penning & Polder (1961), Kambe (1965, 1968), Bonse (1964) and Kato (1963, 1964*a*, *b*). The ray theories examine crystals sufficiently weakly distorted to permit a local reciprocal lattice and dispersion surface to be defined everywhere in the energy-flow triangle. Identification of local wave vectors and Poynting vectors is then possible. These vectors do not appear explicitly in the Takagi-Taupin theory. Clearly, the present problems, which directly involve ray trajectories, fall naturally within the scope of ray theories. Such theories should provide a physical picture of the process of modification of Borrmann-Lehmann interference induced by lattice distortion. However, it is possible to develop a ray theory without explicit expression of phase integrals. This is what Penning & Polder did; and as long as only the tracing of trajectories and the calculation of *Pendellösung*-averaged intensities are the objects of investigation no loss is felt. When dealing with interference phenomena, on the other hand, phase information is necessary. Kato's Eikonal theory is directly informative in this respect. The results of this theory will be applied here, with notation as in Kato (1974).

The function of strain gradients that measures departure from perfect-crystal conditions for the Bragg reflection g is likened by Kato to a 'force', f, and is [Kato, 1974, equation (5-138*a*)]

$$f(x, z) = \pi \left[\cot \theta_B \frac{\partial^2}{\partial z^2}[\bar{\mathbf{g}} \cdot \mathbf{u}(\mathbf{r})] - \tan \theta_B \frac{\partial^2}{\partial x^2}[\bar{\mathbf{g}} \cdot \mathbf{u}(\mathbf{r})] \right] \tag{20a}$$

$$= \frac{\pi}{d}\left[\cot \theta_B \frac{\partial^2 u_g}{\partial z^2} - \tan \theta_B \frac{\partial^2 u_g}{\partial x^2} \right]. \tag{20b}$$

Here $\mathbf{u}(\mathbf{r})$ is the displacement vector referred to the perfect-crystal lattice, $\mathbf{u}(\mathbf{r}) = \mathbf{r} - \mathbf{r}$ (perfect); $\bar{\mathbf{g}}$ is the reciprocal-lattice vector in the perfect crystal, $d = |\bar{\mathbf{g}}|^{-1}$; and u_g is the component of $\mathbf{u}(\mathbf{r})$ parallel to $\bar{\mathbf{g}}$. The rectangular axes x and z are taken in the plane of incidence, as shown in Fig. 10, with origin at O and x parallel to $\bar{\mathbf{g}}$. From his Eikonal theory Kato derives the ray equation

$$\frac{\mathrm{d}}{\mathrm{d}z}\left[\frac{p}{(1-p^2)^{1/2}}\right] = \pm \pi^{-1} \xi_g \tan \theta_B f(x, z) \tag{21}$$

with positive and negative signs applying to branch (1) and branch (2) waves, respectively. Introducing the deviation parameter $w = \pm p(1-p^2)^{-1/2}$, and substituting for f from (20*b*) gives

$$\frac{\mathrm{d}w}{\mathrm{d}z} = \left[\frac{\partial^2 u_g}{\partial z^2} - \tan^2 \theta_B \frac{\partial^2 u_g}{\partial x^2}\right] \Big/ \left(\frac{d}{\xi_g}\right) \tag{22a}$$

in which no $\pm$ sign is needed. Recall that $2d/\xi_g$ is the full width at half-maximum intensity of the Bragg reflection g in the symmetrical Laue case, zero absorption, and is a measure of insensitivity to 'force'. Henceforth the quotient on the right-hand side of (22*a*) will be denoted by $A(x, z) = \pi^{-1} \xi_g \tan \theta_B f(x, z)$ and the equation becomes simply

$$\mathrm{d}w/\mathrm{d}z = A(x, z). \tag{22b}$$

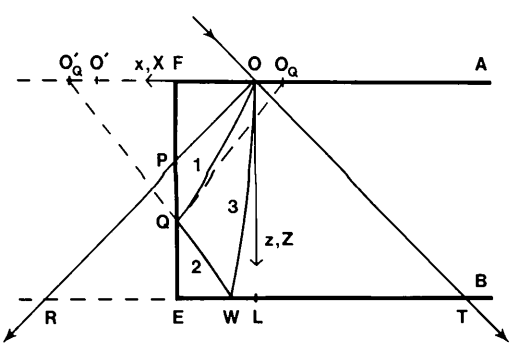

Fig. 10. Curved ray trajectories in the distorted crystal. Type I, negative setting, *cf.* Fig. 1(*a*). Direction of curvature corresponds to f positive and branch (1) rays. [Branch (2) rays not shown]. Drawn for $\tan \theta_B = 1$ to make $x/X = z/Z$. On BE, $z = t$ and $Z = Z_a = At$. At Q, tangent to ray (1) is QO_Q, and tangent to ray (2) is QO'_Q.

How $A(x, z)$ varies in the specimen is unknown. The assumption that A is a constant throughout the energy-flow triangle is hardly realistic, especially in the important corner region near E where two free surfaces FE and BE meet. Strain gradients in the specimen bulk arise from variations of lattice parameter normal to the {111} growth surfaces, and these surfaces outcrop obliquely at the {100} polished free surfaces. However, in order to proceed, constant $A(x, z)$ will now be assumed. Integration of (22b) then gives

$$w - w_e = Az, \tag{23}$$

where w_e is the deviation parameter of the ray concerned at $z = 0$, on the entrance surface. Equations (22b) and (23) show that wave points on both branches of the dispersion surface migrate at constant rate through the Brillouin zone boundary with increasing z. Since the rays are normal to the dispersion surfaces, which are hyperbolic, the rays themselves follow hyperbolic trajectories, which are derivable as follows. Making use of the relation $\mathrm{d}x = \tan\theta_B p\,\mathrm{d}z$ and confining attention to branch (1) rays for which $p = +w(1+w^2)^{-1/2}$, integration of (23) yields

$$A\cot\theta_B x = [1+(Az+w_e)^2]^{1/2} - (1+w_e^2)^{1/2}. \tag{24}$$

Re-arrangement of (24) produces equation (5-155b) of Kato (1974), which is

$$(X+X_0)^2 - (Z+Z_0)^2 = 1, \tag{25}$$

where $X = A\cot\theta_B x$, $Z = Az$, $X_0 = (1+w_e^2)^{1/2}$ and $Z_0 = w_e$. Properties of the family of hyperbolic trajectories represented by (25) are described by Kato (1964b, 1974).

The implications of curved trajectories for Borrmann–Lehmann interference can be visualized from Fig. 10. The first question to be answered in these circumstances is how to satisfy the boundary conditions at Q with an imaginary source on the left of FE. The source should provide a wave of amplitude equal in magnitude to that of the G wave on the right of FE but with reversed x component of Poynting vector so that $p_Q(2) = -p_Q(1)$, signifying by p_Q the local values of p at Q for rays (1) and (2). If the crystal were perfect $p_Q(1)$ would be the ray parameter in an energy-flow triangle with apex at O_Q lying on the tangent to the ray at Q, *i.e.* with $FO_Q/FQ = \tan\theta_B p_Q(1)$. Similarly, $p_Q(2)$ is the ray parameter in a perfect-crystal energy-flow triangle with apex at O'_Q, with $FO'_Q = FO_Q$. The amplitude of the actual G wave within the crystal at Q will differ from that in the perfect-crystal case, so the strength of the imaginary source at O'_Q should also differ from that at O. With small amounts of ray bending, as at present considered, such amplitude differences will be small unless anomalous transmission is very important, and these differences will be disregarded here. Concerning the positions of O_Q and O'_Q, note that rays become increasingly rigid as they approach the directions OR and OT. Hence for rays reflected at P there will be no image source displacement. The displacement $O'O'_Q$ increases steadily as Q moves down to E where it has its maximum value, which is calculated below.

To find the magnitudes of the wavevectors that interfere at W, the local values of p on EB (denoted by p_a) for rays such as (2) and (3) are required. To illuminate such calculation, consider the special ray (not drawn in Fig. 10) that reaches EB at L, the mid-point of RT. By symmetry, $p_a(L) = -p_e$ on the hyperbola concerned and the centre of this hyperbola will lie on the line $Z = \frac{1}{2}Z_a$. Now on any hyperbola belonging to the family given by (25), $p = \mathrm{d}X/\mathrm{d}Z = (Z+Z_0)/(X+X_0)$, and the coordinates of the hyperbola centre are $X = -X_0$, $Z = -Z_0$, with $X_0^2 + Z_0^2 = 1$. So for the hyperbola of the branch (1) ray passing through O and L, $X_0 = \frac{1}{2}(4+Z_a^2)^{1/2}$, and

$$p_a(L) = Z_a(4+Z_a^2)^{-1/2}. \tag{26}$$

When Z_a becomes large, $p_a(L)$ tends to unity, as expected. When $Z_a^2 \ll 1$, $p_a(L) = \frac{1}{2}Z_a$, as could also be derived from (23). Only a rough estimate can be made concerning a likely value of Z_a in the specimen studied. The factor by which *Pendellösung* fringe spacings are contracted in a distorted crystal with constant f is given by equation (5-165b) of Kato (1974), and is $[1+(1/24)Z_a^2]$ at the mid-point of RT. Experiments involving *Pendellösung* fringe spacing measurements in a region about 1 mm distant from FE suggested that the condition $(1/24)Z_a^2 < 0{\cdot}01$ was probably satisfied, making $Z_a^2 \leq 0{\cdot}25$. Call Δp_a the deviation of p from the perfect-crystal value at any point on EB. Then, provided that the conditions $Z_a^2 \ll 1$ and $w_e^2 \ll 1$ are both satisfied, it is easily shown that Δp_a can be taken as constant, approximately $\frac{1}{2}Z_a$ for branch (1) and $-\frac{1}{2}Z_a$ for branch (2) rays. Note that in the type I (negative setting) illustrated in Fig. 10, a ray becomes tangent to FE at E when $\Delta p_a = -P_E$. Here P_E is the geometric constant $a/t\tan\theta_B$, and equals p_E, the perfect-crystal value of p at E, as used in (11b) of § 3. Furthermore, no ray belonging to that branch of the dispersion surface for which $\Delta p_a < -P_E$ can reach E.

The effect of image-source-point shift on fringe spacings can be calculated easily in the case of intra-branch interference by applying (11b) with the perfect-crystal p_E replaced by $P_E + \Delta p_a$, or can be found directly by adding to the distance a the image-source shift, which is $\frac{1}{2}Z_a t\tan\theta_B = \frac{1}{2}At^2\tan\theta_B$. [Addition applies in the setting of Fig. 10, and branch (1) rays.] The fringe spacing given by (13) is changed to

$$\Delta_a = \xi_g(t/a)\tan^2\theta_B/[1\pm(Z_a/2P_E)]. \tag{27}$$

As just stated, the positive sign applies to branch (1) rays and the type I setting. Sign change accompanies change to type II setting or change of branch. Since

typical values of P_E are in the range 0·1 to 0·4, and Z_a may have a magnitude of several tenths in a crystal considered perfect by standard topographic criteria, large relative changes in Δ_a are understandable. In the low-absorption case the opposite effects on branch (1) and branch (2) waves would roughly cancel out when $|Z_a| \ll 2P_E$. When this condition is not satisfied, it can be expected that the smaller of the two periodicities will stand out on topographs, since it will show more fringes in a given distance from E along EB. Quite possibly $|Z_a|/2P_E$ may exceed unity. Then only rays belonging to the dispersion surface branch that increases the denominator on the right-hand side of (27) can produce fringes, as follows from the tangency condition pointed out above. Statistically, therefore, observed Δ_a values less than theoretical might be expected to be found more frequently than values greater, in experiments on crystals containing distortion, just as a geometrical consequence of ray curvature.

In his Eikonal theory, Kato identified a kinetic term T and a potential term $\tilde{N}$ in the phase integrals S taken along ray trajectories in distorted crystals [Kato, 1974, equations (5-131), (5-134)]. In particular, he calculated the contributions of T and $\tilde{N}$ to $S^{(1)} - S^{(2)}$, the phase difference between branch (1) and branch (2) waves, changes in which produced the observed contraction of *Pendellösung* fringe spacings in distorted crystals (Kato, 1964*b*, 1974; Kato & Ando, 1966). Present concern is with the contributions of T and $\tilde{N}$ to $S - S'$, S being the phase integral along the path OW, ray (3), and S' that along the path OQW, ray (1)+(2). [In the perfect-crystal case $S - S'$ is simply the right-hand side of (11).] Discussion will be restricted to the conditions $Z_a^2 \ll 1$, $P_E^2 \ll 1$, and only fringes close to E will be considered, *i.e.* b small, $B^2 \ll 1$. Again, confining attention to intrabranch interference, recall from (12*a*) and (13) that in perfect crystals the fringe reciprocal spacing Δ_a^{-1} is given by

$$\Delta_a^{-1} = \frac{\mathrm{d}}{\mathrm{d}b}[(S - S')/2\pi] = (\xi_g \tan \theta_B)^{-1} P_E. \quad (28)$$

The replacement of P_E by $P_E + \Delta p_a$ in the distorted-crystal case has already been established. Here the need for additional terms on the right-hand side of (28) is investigated. First consider T. In the perfect crystal, integrating along a straight ray between O and W gives [for branch (1)] T (perfect) = $\pi t \xi_g^{-1}(1 - \sigma_w^2)$, with $\sigma = \mathbf{LW}/\mathbf{LR}$, as defined in § 3. Integration along the curved ray (3) gives T (distorted) = $\pi t \xi_g^{-1}[1 - \sigma_w^2 - (1/24)Z_a^2]$. Since the change in T does not depend on σ_w, $S - S'$ is unaffected. Note a significant difference compared with *Pendellösung* interference, where change in T due to distortion changes $S^{(1)} - S^{(2)}$ by the factor $[1 - (1/24)Z_a^2]$ at the centre of the pattern, $\sigma = 0$.

Table 1. *Signs to be attached to the potential term and to the image-source-shift term in equation* (30) *under various experimental conditions*

A positive sign acts to decrease the Borrmann-Lehmann fringe spacing.

Setting		Type I	Type II
Sign of f		+ −	+ −
Potential	Branch (1)	+ −	− +
	Branch (2)	+ −	− +
Image source shift	Branch (1)	+ −	− +
	Branch (2)	− +	+ −

Consider the potential term $\tilde{N}$. Note first that this term is zero in the perfect crystal. Calling $\mathrm{d}l$ a line element of the trajectory along which the integration giving $\tilde{N}$ is taken, it follows from Kato's equations (5-134) and (5-138*a*) that curl $(\mathrm{d}\tilde{N}/\mathrm{d}l) = f$. Hence, as pointed out by Kato (1974, p. 410), application of Stokes's theorem enables the difference in line integrals, $\tilde{N} - \tilde{N}'$, to be converted to the area integral $\int f \, \mathrm{d}x \, \mathrm{d}z$, or simply to $f \int \mathrm{d}x \, \mathrm{d}z$ when f is constant. In the present problem $\int \mathrm{d}x \, \mathrm{d}z$ is the area enclosed by rays OW and OQW and has a positive value since the line integral $OWQO$ is taken clockwise. Straight rays would give $\int \mathrm{d}x \, \mathrm{d}z = tab/(a+b)$, or tb for small b. The curved rays have curvature in the same sense, and so similar in magnitude when b is small that it is quite adequate to set $\int \mathrm{d}x \, \mathrm{d}z = tb$ for them also. Thus $\tilde{N} - \tilde{N}' = ftb$ and

$$\frac{\mathrm{d}}{\mathrm{d}b}[(\tilde{N} - \tilde{N}')/2\pi] = (\xi_g \tan \theta_B)^{-1}(\tfrac{1}{2}Z_a). \quad (29)$$

This contribution to $\mathrm{d}(S - S')/2\pi \, \mathrm{d}b$ matches in magnitude that produced by image-source shift, discussed above. Note the important difference from the latter in that the sign of $\tilde{N} - \tilde{N}'$ is the same for rays belonging to both branches (1) and (2). [This can be understood by recognizing that the integral $\tilde{N}$ is just a geometrical result of the path taken through the field $\mathbf{u}(\mathbf{r})$.] It is also important to note that the contribution to $S - S'$ depends upon the first power of Z_a. This contrasts with the corresponding contribution of $\tilde{N}^{(1)} - \tilde{N}^{(2)}$ to $S^{(1)} - S^{(2)}$ in the distorted-crystal *Pendellösung* pattern, when it is proportional to Z_a^2; and at the centre of the pattern the contribution $\tilde{N}^{(1)} - \tilde{N}^{(2)}$ increases the perfect-crystal value of $S^{(1)} - S^{(2)}$ by the factor $[1 + (1/12)Z_a^2]$. For Borrmann-Lehmann fringes, in the case of the type I setting and branch (1) rays, the fringe spacing given by (13) is now modified to

$$\Delta_a = \xi_g (t/a) \tan^2 \theta_B [1 + (Z_a/2P_E) + (Z_a/2P_E)]^{-1} \quad (30)$$

when the contributions of both image-source shift and $\tilde{N} - \tilde{N}'$ are included on the right-hand side. Table 1 sets out the signs that should be assigned to the two terms of magnitude $Z_a/2P_E$ in this equation under

the various combinations of experimental conditions that may be encountered.

The foregoing analysis has uncovered diffraction-theoretical reasons to account for the observations of large relative changes of Borrmann–Lehmann fringe spacings produced by strain gradients too small to affect *Pendellösung* spacings noticeably in a conventional topograph. In all but the most perfect crystals, $Z_a/2P_E$ is unlikely to be small compared with unity. For example, if f arose from a uniform dilatation gradient normal to the Bragg planes, then a gradient as low as 10^{-6} mm^{-1} would make $Z_a \simeq 0{\cdot}1$ when diffraction parameters similar to those operating in the experiments illustrated in § 4 applied. Then with small values of P_E, about 0·1 say, changes in fringe spacing of order 100% would be produced. This analysis justifies the suggestion previously made (Lang *et al.*, 1986) that experiments of the Borrmann–Lehmann interference type deserve serious consideration for development and application in crystal assessment work. The origin of the high sensitivity may be qualitatively pictured by an analogy with X-ray interferometry. It can be said that the action of combining rays *OW* and *OQW*, which take quite different paths through the distorted crystal, turns the specimen into its own interferometer.

The authors thank the Director and Staff of the SERC Daresbury Laboratory for the provision of experimental facilities, and SERC for financial support. One of the authors (GK) was also sponsored by the Polish Ministry of National Education within Project CPBP01.06. Experimental assistance by Dr Moreton Moore, University of London Royal Holloway and Bedford New College, is gratefully acknowledged.

References

BONSE, U. (1964). *Z. Phys.* **177**, 385-423.
BORRMANN, G. & LEHMANN, K. (1963). *Crystallography and Crystal Perfection*, edited by G. N. RAMACHANDRAN, pp. 101-108. London, New York: Academic Press.
DAWSON, B. (1967). *Proc. R. Soc. London Ser. A*, **298**, 264-288.
HART, M. & LANG, A. R. (1965). *Acta Cryst.* **19**, 73-77.
HATTORI, H., KURIYAMA, H. & KATO, N. (1965). *J. Phys. Soc. Jpn*, **20**, 1047-1050.
KAMBE, K. (1965). *Z. Naturforsch. Teil A*, **20**, 770-786.
KAMBE, K. (1968). *Z. Naturforsch. Teil A*, **23**, 25-43.
KATO, N. (1961*a*). *Acta Cryst.* **14**, 526-532.
KATO, N. (1961*b*). *Acta Cryst.* **14**, 627-636.
KATO, N. (1963). *J. Phys. Soc. Jpn*, **18**, 1785-1791.
KATO, N. (1964*a*). *J. Phys. Soc. Jpn*, **19**, 67-77.
KATO, N. (1964*b*). *J. Phys. Soc. Jpn*, **19**, 971-985.
KATO, N. (1968). *J. Appl. Phys.* **39**, 2231-2237.
KATO, N. (1974). In *X-ray Diffraction*, by L. V. AZÁROFF, R. KAPLOW, N. KATO, R. J. WEISS, A. J. C. WILSON & R. A. YOUNG, Chs. 4, 5. New York: McGraw-Hill.
KATO, N. & ANDO, Y. (1966). *J. Phys. Soc. Jpn*, **21**, 964-968.
KOWALSKI, G. & LANG, A. R. (1986). *J. Appl. Cryst.* **19**, 224-228.
KOWALSKI, G. & LANG, A. R. (1987). *Acta Cryst.* A**43**, C220.
LANG, A. R. (1957). *Acta Metall.* **5**, 358-364.
LANG, A. R. (1983). *Rev. Sci. Instrum.* **54**, 897-899.
LANG, A. R., KOWALSKI, G., MAKEPEACE, A. P. W. & MOORE, M. (1986). *Acta Cryst.* A**42**, 501-510.
LEHMANN, K. & BORRMANN, G. (1967). *Z. Kristallogr.* **125**, 234-248.
MAI, Z.-H. & ZHAO, H. (1989). *Acta Cryst.* A**45**, 602-609.
PENNING, P. & POLDER, P. (1961). *Philips Res. Rep.* **16**, 419-440.
SAKA, T., KATAGAWA, T. & KATO, N. (1972*a*). *Acta Cryst.* A**28**, 102-113.
SAKA, T., KATAGAWA, T. & KATO, N. (1972*b*). *Acta Cryst.* A**28**, 113-120.
TAKAGI, S. (1962). *Acta Cryst.* **15**, 1131-1132.
TAKAGI, S. (1969). *J. Phys. Soc. Jpn*, **26**, 1239-1253.
TAUPIN, D. (1964). *Bull. Soc. Fr. Minéral. Cristallogr.* **87**, 469-511.

Acta Cryst. (1990). A**46**, 227-233

Direct Calculation of Unambiguous Electron-Density Distributions of Langmuir–Blodgett Films Normal to the Membrane Plane

BY MATTHIAS VON FRIELING AND HANS BRADACZEK

Institut für Kristallographie, Freie Universität Berlin, Takustrasse 6, *D*-1000 *Berlin* 33, *Federal Republic of Germany*

(*Received* 7 *July* 1989; *accepted* 16 *October* 1989)

Abstract

In regard to X-ray diffraction, Langmuir–Blodgett (LB) films consisting of lipid bilayers represent a 'one-dimensional crystal' with a very small number of unit cells in the direction of stacking. Such bounded systems yield X-ray diffraction diagrams which, in certain respects, contain more information than those of the conventional effectively infinite single crystals. This additional information consists of the profiles of the broadened reflections and their dislocation from the reciprocal-lattice points. These profiles are specific for each different structure and hence enable the direct calculation of unambiguous electron-density distributions from a single set of intensity data. At first, the Q function (the generalized Patterson function), *i.e.* the distance statistics of the structure sought after is calculated from the intensity data.

0108-7673/90/030227-07$03.00 © 1990 International Union of Crystallography